

Condensates in thin-layer turbulence

Adrian van Kan^{1,2†}, Alexandros Alexakis²

¹Fakultät für Physik und Astronomie, Universität Heidelberg, Im Neuenheimer Feld 226,
D-69120 Heidelberg, Germany

²Laboratoire de Physique Statistique, Département de Physique de l'Ecole Normale Supérieure, PSL Research University, Université Paris Diderot, Sorbonne Paris Cité, Sorbonne Universités, UPMC Univ. Paris 06, CNRS, 75005 Paris, France

(Received 3 August 2018; revised 3 August 2018; accepted 3 August 2018)

We examine the steady state of turbulent flows in thin layers using direct numerical simulations. It is shown that when the layer thickness is smaller than a critical height, an inverse cascade arises which leads to the formation of a steady state condensate where most of the energy is concentrated in the largest scale of the system. For layers of thickness smaller than a second critical height, the flow at steady state becomes exactly two-dimensional. The amplitude of the condensate is studied as a function of layer thickness and Reynolds number. Bi-stability and intermittent bursts are found close to the two critical points. The results are interpreted based on a three-scale model that reproduces the basic features of the numerical results.

Key words:

1. Introduction

Turbulent flows in geophysical and astrophysical contexts are often subject to geometrical constraints, such as thinness in a particular direction, that can strongly affect the behaviour of the flow. This occurs, for instance, in planetary atmospheres and oceans (Pedlosky 2013) whose behaviour can strongly deviate from the classical three-dimensional homogeneous and isotropic turbulence. This is related to the well-known fact that the behaviour of flows at large Reynolds numbers Re depends on the dimensionality of the system. In three dimensions (3D), vortex stretching transfers energy to small scales in a *direct cascade* (Frisch 1995). By contrast, in two-dimensions (2D), the conservation of enstrophy in addition to energy gives rise to an inverse energy cascade, a transfer of energy to the large scales (Boffetta & Ecke 2012). Flows in thin layers share properties of both systems with the large scales behaving like a 2D flow and small scales behaving like a 3D flow. As a result, such systems are known to cascade energy both to large and to small scales (Smith *et al.* 1996). In fact, it has been shown in (Celani *et al.* 2010; Musacchio & Boffetta 2017; Benavides & Alexakis 2017) that as the height of the layer H is varied, the system transitions from a state where energy cascades only to the small scales for large H , to a state where energy cascades to both large and small scales when H is smaller than approximately half the size of the forcing length scale ℓ . In particular, (Benavides & Alexakis 2017), using a Galerkin truncated model of the Navier-Stokes, were able to provide strong evidence of the criticality of the transition. In addition, they observed a second transition to exact two-dimensionalisation for layers of very small thickness H

† Email address for correspondence: adrien.van.kan@ens.fr

$H \propto \ell Re^{-1/2}$. This transition had been predicted theoretically using bounding techniques by (Gallet & Doering 2015). Similar transitions from a strictly forward cascade to an inverse cascade have been observed in other systems like rotating turbulence (Deusebio *et al.* 2014), stratified turbulence (Sozza *et al.* 2015), rotating and stratified flows (Marino *et al.* 2015) magneto-hydrodynamic systems (Alexakis 2011; Seshasayanan *et al.* 2014; Seshasayanan & Alexakis 2016) and helically constrained flows (Sahoo & Biferale 2015; Sahoo *et al.* 2017), to mention a few. The thin layer however remains possibly the simplest model exhibiting such transitions and it thus deserves a detailed study at the different stages of the inverse cascade evolution.

In the presence of an inverse cascade, for finite systems and in the absence of a large-scale dissipation term, there are two stages in the development of the flow. In the first stage (at early times), energy is transferred to larger and larger scales by the inverse cascade. This process stops, however, when scales comparable to the system size are reached, after which energy starts to pile up at these largest scales. In the long-time limit, the increase of the large-scale energy saturates and a condensate is formed, where nearly all energy is found in the first few Fourier modes. In terms of the real space flow field, this spectral condensation corresponds to coherent system-size vortices or shear layers Frishman & Herbert (2017); Frishman *et al.* (2017); Bouchet & Simonnet (2009). In 2D, where the cascade of energy is strictly inverse, a steady state in the condensate regime is realised when the energy of the condensate is so large that the dissipation due to viscosity at large scales balances the energy injection due to the forcing. For split cascading systems, this is not necessarily true since other processes exist that can redirect the energy back to the small scales where viscous dissipation is more efficient. Such mechanisms have been demonstrated for rotating turbulence, where a flux-loop mechanism has been identified (cf. Bartello *et al.* 1994; Seshasayanan & Alexakis 2018; Alexakis 2015; Yokoyama & Takaoka 2017). Similarly, the turbulent condensate in a three-dimensional thin layer may differ from the two-dimensional case due to the presence of non-vanishing 3D flow variations associated with the direct cascade.

The previous studies of the thin-layer problem have focused on the transient growth of total kinetic energy due to the inverse cascade. By contrast, the condensate state reached after long time in the thin-layer case has not yet been examined due to the long computation time needed. In this study, we aim to fill this gap and investigate the behaviour of turbulent flow at the condensate stage for a thin layer forced at intermediate scales, using direct numerical simulations (DNS) and low-order modelling. The DNS provide a detailed picture of the behaviour of the full system, while the modelling shines light on the main physical processes involved in the problem.

The remainder of this article is structured as follows. In section 2, we present the set-up and define the quantities we will be measuring. In section 3, we present the results of a large number of direct numerical simulations (DNS) of thin-layer turbulence. Next, in section 4, we discuss the behaviour close to the two critical points and in section 5, we present spectra and spectral fluxes of energy. In section 6, we introduce a low-order model which captures many features of the DNS results. Finally, in section 7, we discuss our results and summarise.

2. Physical setup

In this section, we describe the set-up to be investigated. We consider the idealised case of forced incompressible three-dimensional flow in a triply periodic box of dimensions $L \times L \times H$. The thin direction H will be referred to as the *vertical* ‘ z ’ direction and the

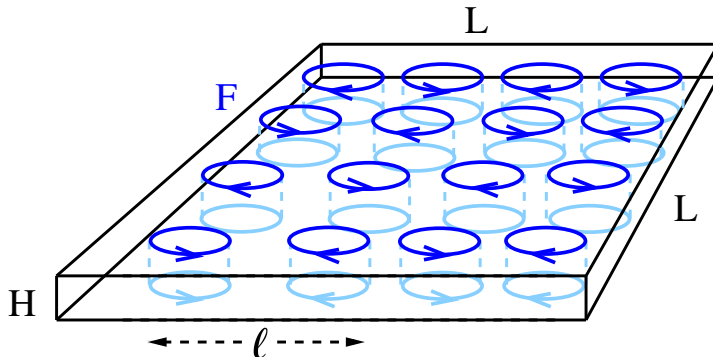


Figure 1: The domain used is a box of height H and square base of side length L . The forcing is invariant along the thin direction and stochastic with fixed mean rate of energy input, while involving only wavenumbers \mathbf{k} with $|\mathbf{k}| = k_f = 2\pi/\ell$. The thin direction will be referred to as the *vertical*, the others as the *horizontal* directions.

remaining two as the *horizontal* 'x' and 'y' directions. The geometry of the domain is illustrated in figure 1. The flow follows the incompressible Navier-Stokes equation:

$$\partial_t \mathbf{u} + \mathbf{u} \cdot \nabla \mathbf{u} = -\nabla P + \nu \nabla^2 \mathbf{u} + \mathbf{f}, \quad (2.1a)$$

$$\nabla \cdot \mathbf{u} = 0 \quad (2.1b)$$

where \mathbf{u} is the velocity field, P is physical pressure divided by constant density and ν is (kinematic) viscosity. Energy is injected into the system by the stochastic force \mathbf{f} that depends only on x and y and has only x and y components, i.e. it is a two-dimensional-two-component (2D2C) field. The force is divergence-free, hence it can be written as $\mathbf{f} = (-\partial_y \psi, \partial_x \psi, 0)$. The spectrum of \mathbf{f} is concentrated in a ring of wavenumbers of radius $k_f \equiv 2\pi/\ell$. It is delta-correlated in time, which leads to a fixed injection of energy $\langle \mathbf{u} \cdot \mathbf{f} \rangle = \epsilon$, where $\langle \cdot \rangle$ denotes an ensemble average over infinitely many realisations. We use random initial conditions whose small energy is spread out over a range of wave numbers. In some cases, in order to compare with previous studies, we used a hyper-viscosity, which amounts to replacing $\nu \nabla^2 \mathbf{u}$ by $-\nu_n (-\nabla^2)^n \mathbf{u}$.

The system (2.1) is characterised by three non-dimensional parameters: the Reynolds number based on the energy injection rate $Re = (\epsilon \ell^4)^{1/3} / \nu$, the ratio between forcing scale and domain height $Q = \ell / H$ and the ratio between forcing scale and the horizontal domain size $K = \ell / L$. The ratio between K and Q gives the aspect ratio $A = K / Q = H / L$ of the domain. The Kolmogorov dissipation length is denoted as $\eta = \nu^{3/4} / \epsilon^{1/4} = \ell Re^{3/4}$.

The simulations performed for this work used an adapted version of the Geophysical High-Order Suite for Turbulence (GHOST) which uses pseudo-spectral methods including 2/3 aliasing to solve for the flow in the triply periodic domain, (see Mininni *et al.* 2011). The resolution was varied from $256^2 \times 16$ grid points to $2048^2 \times 128$ grid points depending on the value of the parameters. To explore the space spanned by these three parameters, we have performed systematic numerical experiments: for a fixed value of Re and $K = 1/8$, different simulations are performed with Q varying from small to large values. The runs are continued until a steady state is reached where all quantities fluctuate around their mean value. This is repeated for eight different values of Re from $Re = 203$ (resolution $256^2 \times 16$) to 4062 (resolution $2048^2 \times 128$) and for one value of

Re	203	305	406	609	870	2031	4062	Hyper
$1/K$	8	8 & 16	8	8	8	8	8	8
$n_x = n_y$	256	256 & 512	256	512	512	1024	2048	1024
n_z	16	16	16	32	32	64	128	64
# runs	40	40	40	30	30	10	2	4

Table 1: Summary of the different runs performed. For each Re and K several runs for different values of Q have been performed. The horizontal resolution is n_x, n_y , while n_z stands for the vertical resolution at $Q = 2$. The vertical resolution was changed with Q to maintain an isotropic grid, $Kn_x = Kn_y = Qn_z$ wherever possible.

hyperviscosity ($n = 8, \nu_8 = 10^{-38}$ as in (Celani *et al.* 2010)), as a consistency check, since many of the previous studies of thin-layer turbulence used hyper-viscosity. For $Re = 305$, we also perform a run with $K = 1/16$ ($L \rightarrow 2L$). The number of runs performed for each Re are summarised in table 1.

To quantify the energy distribution among different scales it is convenient to work in Fourier space. The Fourier series expansion of the velocity reads

$$\mathbf{u}(\mathbf{x}, t) = \sum_{\mathbf{k}} \hat{\mathbf{u}}_{\mathbf{k}} e^{i\mathbf{k}\cdot\mathbf{x}}, \quad \hat{\mathbf{u}}_{\mathbf{k}} = \frac{1}{L^2 H} \int \mathbf{u}(\mathbf{x}, t) e^{-i\mathbf{k}\cdot\mathbf{x}} d\mathbf{x} \quad (2.2)$$

where $\hat{\mathbf{u}}_{\mathbf{k}} = (\hat{u}_{\mathbf{k}}^{(x)}, \hat{u}_{\mathbf{k}}^{(y)}, \hat{u}_{\mathbf{k}}^{(z)})$ and the sum runs over all $\mathbf{k} \in (\frac{2\pi}{L}\mathbb{Z})^2 \times \frac{2\pi}{H}\mathbb{Z}$. In the pseudo-spectral calculations, this sum is truncated at a finite k_{res} . Since flow in a thin layer is a highly anisotropic system, it is important to consider quantities in the vertical and horizontal directions separately. For this purpose, we monitor various quantities in our simulations. Firstly, different energy spectra, namely the total energy spectrum as a function of horizontal wavenumber k_h

$$E(k_h) = \frac{1}{2} \sum_{\substack{\mathbf{k} \\ k_x^2 + k_y^2 = k_h^2}} |\hat{\mathbf{u}}_{\mathbf{k}}|^2, \quad (2.3)$$

the energy spectrum of the (vertically averaged) 2D2C field

$$E_h(k_h) = \frac{1}{2} \sum_{\substack{\mathbf{k} \\ k_x^2 + k_y^2 = k_h^2 \\ k_z = 0}} \left(|\hat{u}_{\mathbf{k}}^{(x)}|^2 + |\hat{u}_{\mathbf{k}}^{(y)}|^2 \right), \quad (2.4)$$

the energy spectrum of the (vertically averaged) vertical velocity

$$E_z(k_h) = \frac{1}{2} \sum_{\substack{\mathbf{k} \\ k_x^2 + k_y^2 = k_h^2 \\ k_z = 0}} \left| \hat{u}_{\mathbf{k}}^{(z)} \right|^2, \quad (2.5)$$

and the energy spectrum of the 3D flow defined as

$$E_{3D}(k_h) = \frac{1}{2} \sum_{\substack{\mathbf{k} \\ k_x^2 + k_y^2 = k_h^2 \\ k_z \neq 0}} |\hat{\mathbf{u}}_{\mathbf{k}}|^2. \quad (2.6)$$

Furthermore, we monitor different components of domain-integrated energy, namely the total horizontal kinetic energy

$$\frac{1}{2}U_h^2 = \frac{1}{2} \sum_{\substack{\mathbf{k} \\ k_z=0}} \left(\left| \hat{u}_{\mathbf{k}}^{(x)} \right|^2 + \left| \hat{u}_{\mathbf{k}}^{(y)} \right|^2 \right) \quad (2.7)$$

(based on the (vertically averaged) 2D2C field only), the large-scale horizontal kinetic energy

$$\frac{1}{2}U_{ls}^2 = \frac{1}{2} \sum_{\substack{\mathbf{k} < k_{max} \\ k_z=0}} \left(\left| \hat{u}_{\mathbf{k}}^{(x)} \right|^2 + \left| \hat{u}_{\mathbf{k}}^{(y)} \right|^2 \right), \quad (2.8)$$

where $k_{max} = \sqrt{2} \frac{2\pi}{L}$, as well as the (vertically averaged) large-scale kinetic energy in the z component

$$\frac{1}{2}U_z^2 = \frac{1}{2} \sum_{\substack{\mathbf{k} < k_{max} \\ k_z=0}} \left| \hat{u}_{\mathbf{k}}^{(z)} \right|^2 \quad (2.9)$$

and the three-dimensional kinetic energy (*3D energy*), defined as

$$\frac{1}{2}U_{3D}^2 = \frac{1}{2} \sum_{k_z \neq 0} \left| \hat{\mathbf{u}}_{\mathbf{k}} \right|^2. \quad (2.10)$$

Finally, we also monitor three different quantities related to spectral energy flux. First, the total energy flux as a function of horizontal wave number

$$\Pi(k_h) = \langle \mathbf{u}_{k_h}^< \cdot (\mathbf{u} \cdot \nabla) \mathbf{u} \rangle, \quad (2.11)$$

where the low-pass filtered velocity field is

$$\mathbf{u}_{k_h}^< = \sum_{\substack{\mathbf{k} \\ k_x^2 + k_y^2 < k_h^2}} \hat{\mathbf{u}}_{\mathbf{k}} e^{i\mathbf{k} \cdot \mathbf{x}}.$$

With this definition, $\Pi(k_h)$ expresses the flux of energy through the cylinder $k_x^2 + k_y^2 = k_h^2$ due to the non-linear interactions. The 2D energy flux as a function of k_h is defined as

$$\Pi_{2D}(k_h) = \langle \bar{\mathbf{u}}_{k_h}^< \cdot (\bar{\mathbf{u}} \cdot \nabla) \bar{\mathbf{u}} \rangle, \quad (2.12)$$

where the over-bar stands for vertical average and expresses the flux through the same cylinder due to only 2D2C interactions. Finally we define the 3D energy flux as a function of horizontal wave number

$$\Pi_{3D}(k_h) = \Pi(k_h) - \Pi_{2D}(k_h). \quad (2.13)$$

It expresses the flux due to all interactions other than the ones in (2.12).

3. Results from the direct numerical simulations

In this section, we present the results obtained from our simulations. For a given set of parameters Re, Q, K , two different behaviours are possible. For thick layers $Q \ll 1$, 3D turbulence is observed, i.e. there is no inverse cascade and the energy injected by the forcing is transferred to the small scales where it is dissipated. No system-size structures appear in this case. For thin layers $Q \gg 1$, a split cascade is present with part of the energy cascading inversely to the large scales and part of the energy cascading forward to the small scales. For these layers, at steady state, coherent system-size vortices appear

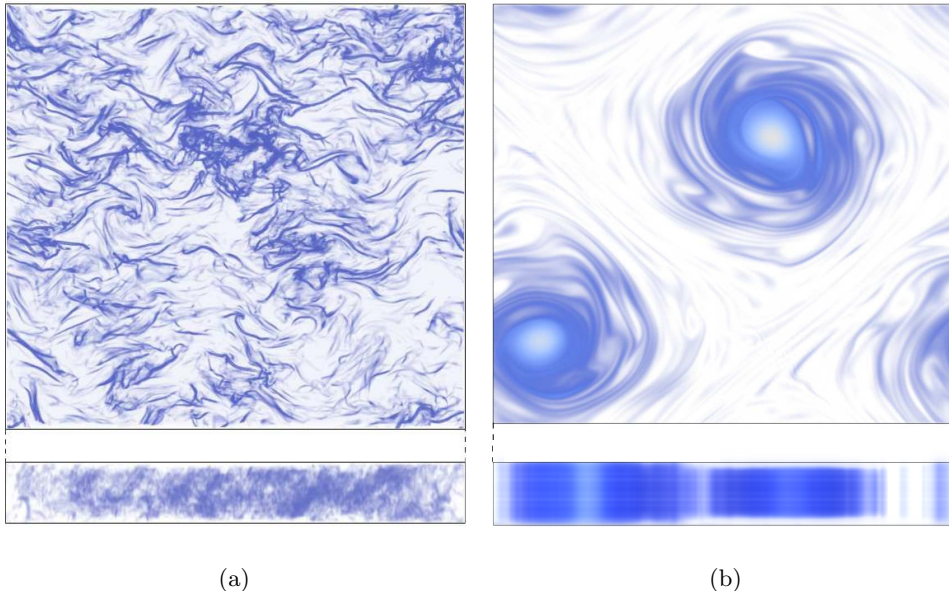


Figure 2: Typical flow fields in the steady state of 3D turbulence (2a) and two-dimensional turbulence (2b) regimes, visualised using squared vorticity. In the 3D turbulence regime, no large-scale organisation is visible, whereas the condensate is characterised by the presence of two counter-rotating system-size vortices. The boxes below show the corresponding side views. In the 3D turbulent state, there are significant variations along the vertical, while in the 2D turbulent state, there is invariance along the z -direction.

with very large amplitudes. A visualisation of the flow field in these two different states is shown in figure 2 for the 3D turbulence state (left) and the condensate state (right). Typical time-series of U_h^2 for a thick layer (green line), in the absence of an inverse cascade, and a thin layer (blue line) in the presence of an inverse cascade are shown in figure 3a. For the thick layer, the total energy fluctuates around a mean value of order $(\epsilon\ell)^{2/3}$, while for the thin layer, the energy saturates to a value much larger than in the thick layer. The energy spectra for the two runs of figure 3a at the steady state are shown in figure 3b, where it is shown quantitatively how much energy is concentrated in the large scales for the two different cases.

In more detail, U_h^2 for the thin layer shows two different stages: first, at early times, there is a linear increase with time and second, there is saturation at late times. Therefore, to fully describe the evolution of the system, we need to quantify the rate of the initial energy increase and the energy at which it saturates. The red **dashed** line indicates a fit to the initial linear increase. This slope provides a measurement of the rate ϵ_{inv} at which energy cascades inversely. For the steady state stage, the black **dashed-dot** line indicates the mean value at late times. For all our runs, we measure the slope of the total horizontal energy increase and the steady state mean values of all corresponding energies defined in the previous section. For the runs of high resolution, to accelerate the convergence to the steady state, the large-scale velocity $\mathbf{u}_{k=1}$ (from a run at the early stage) has been increased artificially and continued. Alternatively an output of another run which had already converged was used as initial condition. However, all cases were run sufficiently long to demonstrate that they have reached a steady state.

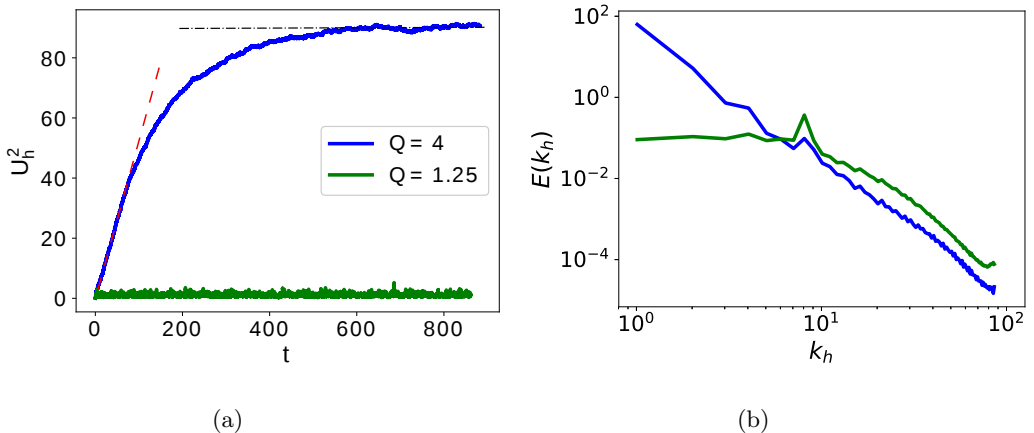


Figure 3: Panel (a) shows the typical time evolution of U_h^2 for $Q = 1.25 < Q_{3D}$ and $Q = 4 > Q_{3D}$. For $Q < Q_{3D}$, the total large-scale energy only fluctuates around a small mean value. For $Q > Q_{3D}$, there is an initially linear increase whose slope corresponds to the rate of inverse energy transfer. In the long-time limit, the large-scale energy reaches its steady state value. Two quantities are measured: the initial slope (red dashed line) and the condensate value (horizontal black dashed-dot line). Panel (b) shows the corresponding spectra: in the presence of an inverse cascade, there is a maximum at the largest scale, while in its absence, the maximum is near the forcing scale.

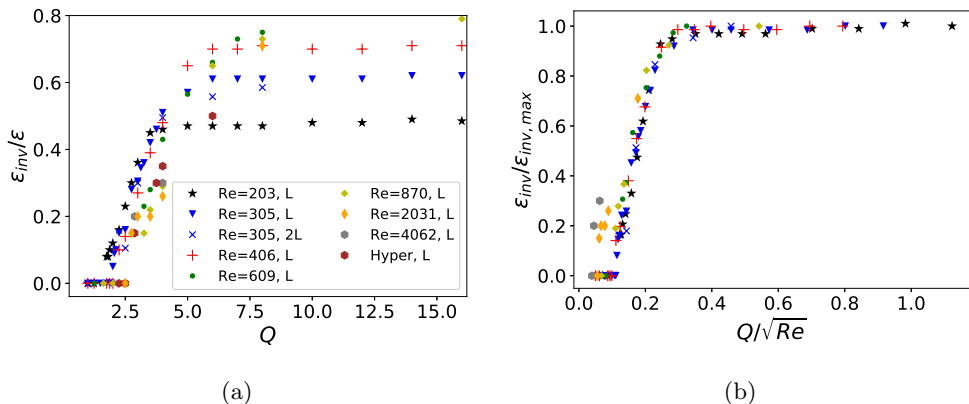


Figure 4: Panel (a): initial slopes, measured as indicated in figure 3a, non-dimensionalised by the energy injection rate ϵ , as a function of Q ($\propto 1/H$) for all Re used. The same symbols will be used in all plots in this section. Thick layers are on the left (small Q) and thin layers on the right (large Q). Panel (b): the same data collapsed by a rescaling of the abscissa by \sqrt{Re} and the coordinate by the maximum value obtained for that Reynolds number.

Figure 4 shows the slopes of the initial total energy increase ϵ_{inv} , measured as illustrated in figure 3a for all our numerical simulations. The slopes are non-dimensionalised by the energy input rate ϵ and plotted versus Q for all different values of Re including the hyper-viscous runs. The slope at this early stage measures the strength of inverse energy transfer. At small Q (deep layers), the slope vanishes for all runs, showing that

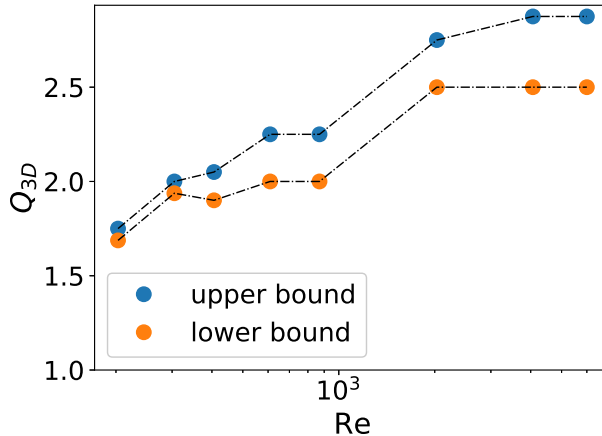


Figure 5: Estimated value of Q_{3D} as a function of Re . the top line shows the smallest value of Q for which an inverse cascade was observed and the bottom line shows the largest value of Q for which no inverse cascade was observed. The rightmost point indicates the results from the hyper-viscous runs.

no inverse cascade is present. Moving to larger Q , for every Re , there is a critical value $Q_{3D}(Re)$ of Q above which the slope becomes non-zero. This is the birth of the inverse cascade. Figure 5 shows estimates of Q_{3D} as a function of Re : the upper curve shows the smallest Q for which an inverse cascade was observed for that given Re while the lower curve shows the largest Q for which no inverse cascade was observed. The critical value Q_{3D} lies between these two curves. The point Q_{3D} shifts to larger Q as Re is increased but eventually for the two largest Re simulated, namely $Re = 2031$ and $Re = 4062$, as well as the hyper-viscous run, Q_{3D} saturates at $Q_{3D} \approx 2.5$. (Previous findings (Celani *et al.* 2010) estimated this value to $Q_{3D} \approx 2$, however in that work too limited a range of values of Q was used to be able to precisely pinpoint Q_{3D} . Another possible reason for the different result is the different value of $1/K$ associated with the different forcing wavenumber $k_f = 16$ used.) The saturation of $Q_{3D} \approx 2.5$ indicates that Q_{3D} converges to this value at large Re . For $Q > Q_{3D}$, the slope begins to increase approximately linearly $\epsilon_{inv} \propto Q - Q_{3D}$.

If Q is increased further, a value Q_{2D} is reached beyond which the slope becomes independent of Q . Above this second critical point, the flow becomes exactly 2D (Benavides & Alexakis 2017). This second critical point Q_{2D} increases with Re as $Q_{2D} \propto Re^{1/2}$. This scaling is verified in this work as well and shown in the right panel of figure 4. These two critical points Q_{3D} and Q_{2D} at this early stage of development of the inverse cascade have been studied in detail in the past (Benavides & Alexakis 2017; Celani *et al.* 2010).

Here we mostly focus on the second stage of evolution: the steady state and the properties of the condensate. Figure 6 shows the equilibrium value of U_h^2 , as defined in equation (2.8), non-dimensionalised by the forcing energy scale $(\epsilon\ell)^{2/3}$ (and multiplied by K^2). In the left panel, it is plotted versus Q (figure 6a) and in the right panel the condensate energy is rescaled by $1/Re$ and plotted versus $\eta/H = QRe^{-3/4}$ (figure 6b). First consider figure 6a. At small Q , there is very little energy in the large scales. This corresponds to the values of Q that displayed no inverse cascade at the initial stage. In the absence of an inverse cascade, the large scales only possess a small non-zero energy

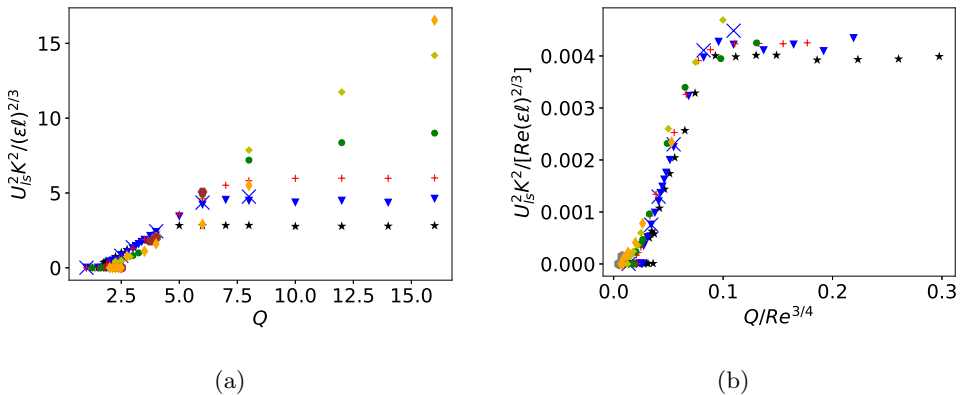


Figure 6: Left panel: U_{ls}^2 as defined in eq. (2.8), nondimensionalised by $(\epsilon l)^{2/3}/K^2$ as a function of Q . Right panel: the same data (excluding the hyper-viscous run), with the large-scale energy rescaled by $1/Re$ and plotted versus $Q/Re^{3/4}$ that shows a satisfactory data collapse. The value $Q_{3D}/Re^{3/4}$ (for which U_{ls}^2 reaches its plateau) coincides for all Re at about $Q/Re^{3/4} \approx 0.09-0.1$.

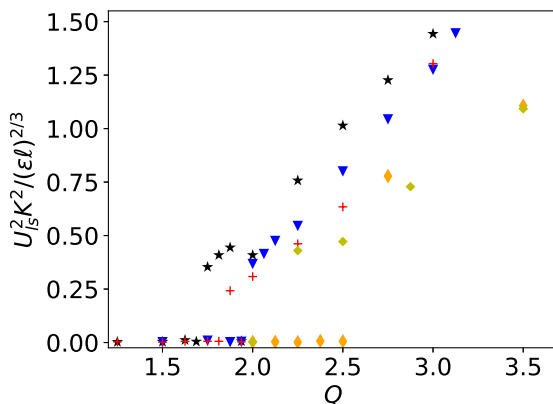


Figure 7: Zoomed-in version of figure 6a showing that there is a discontinuity in $U_{ls}^2/(\epsilon l)^{2/3}$ at Q_{3D} for all Reynolds numbers up to the second highest simulated.

and are expected to be in a thermal equilibrium state (Kraichnan 1973; Cameron *et al.* 2017; Dallas *et al.* 2015). For $Q > Q_{3D}$ the energy in the large scale takes larger values. In all cases, the energy increases nearly linearly $U_{ls}^2 \propto (Q - Q_{3D})$ for $Q_{2D} > Q > Q_{3D}$. The close coincidence of the experiments with $K = 1/8$ and $K = 1/16$ at $Re = 305$, given the choice of coordinate, indicates a scaling of $U_{ls}^2 \propto L^2$. If we zoom in on Q_{3D} (see the figure 7), we observe that there are clear signs of small but discontinuous jumps of U_{ls}^2 at Q_{3D} that are not visible in the zoomed out figure 6a. These cases are examined in more detail in the next section.

The increase of the large-scale energy stops at the second critical point Q_{2D} , where U_{ls}^2 becomes independent of Q . It is noteworthy that the curves for various values of Re all follow the same straight line between their respective Q_{3D} and Q_{2D} with only some

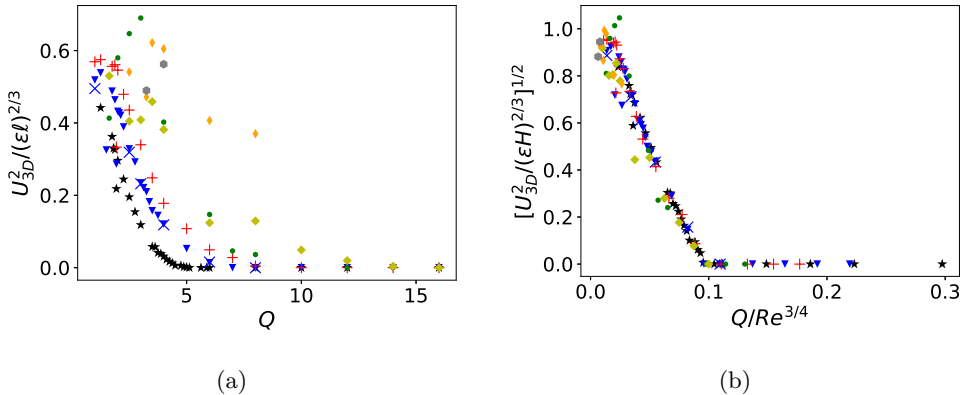


Figure 8: Left panel: U_{3D}^2 as defined in equation (2.10), non-dimensionalised by $(\epsilon \ell)^{2/3}$ and plotted versus Q . Right panel: the same information as figure (8a), but in terms of the square-root of the 3D kinetic energy rescaled by $(\epsilon H)^{2/3}$, plotted versus $Q/Re^{3/4}$. This rescaling indicates that $U_{3D}^2 \propto (Q_{2D} - Q)^2$ close to the transition.

deviations at low Q . Furthermore, both Q_{2D} and the level to which U_{ls}^2 saturates depend on Re . In figure 6b, the same data is plotted, but the axes are rescaled. The rescaling collapses the data well, with some deviations at small Q related to the convergence of Q_{3D} . This indicates that at large values of Q , U_{ls}^2 scales like $U_{ls}^2 \propto (\epsilon \ell)^{2/3} Re$. This is the scaling of the condensate of 2D turbulence (Boffetta & Ecke 2012; Frishman & Herbert 2017). Furthermore, the critical value where the transition to this maximum value of U_{ls}^2 occurs is given by $Q_{2D} Re^{-3/4} = \eta/H_{2D} \approx 0.09 - 0.1$. The scaling used to collapse the data in figure 4 (inverse cascade) is different from that used in figures 6,8 and 9 (condensate state). This implies that $Q_{2D} \propto Re^{1/2}$ estimated during the early stage of the inverse cascade development is different from $Q_{2D} \propto Re^{3/4}$ estimated at steady state where a condensate is formed. The reason for this difference is that the transition to exactly two-dimensional motion will occur when the maximum shear in the flow (which produces 3D motion by shear instabilities) is balanced by small-scale viscous dissipation. In the presence of the inverse cascade, an $E(k) \propto \epsilon^{2/3} k^{-5/3}$ spectrum is formed such that the peak of the enstrophy spectrum $k^2 E(k)$ is at the forcing scale. Thus the balance between 2D shear and 3D damping is

$$(\epsilon \ell)^{1/3} / \ell \sim \nu / H^2,$$

which implies $H_{2D} \sim \ell Re^{-1/2}$ (Benavides & Alexakis 2017). For the condensate state, however, most of the energy and enstrophy are located in the largest scales and are such that energy injection ϵ is balanced by large-scale dissipation $\propto \nu U_{ls}^2 / L^2$. The large-scale shear is thus $U_{ls} / L \propto (\epsilon / \nu)^{1/2}$ which we balance with the damping rate of 3D perturbations,

$$(\epsilon / \nu)^{1/2} \sim \nu / H^2,$$

to obtain the scaling $H_{2D} \propto \epsilon^{1/4} \nu^{3/4} \propto \ell Re^{-3/4}$. We will recover the very same steady state scaling in the section 6 from a simplified three-scale model. These two scalings imply that a flow that becomes exactly 2D at the early stages of the inverse cascade for $Q \gtrsim Re^{1/2}$ might develop 3D instabilities at the condensate state if $Q \lesssim Re^{3/4}$.

Figure 8 shows the three-dimensional energy as defined in equation (2.10). In the left panel it is non-dimensionalised by the forcing energy $(\epsilon \ell)^{2/3}$ and plotted versus Q (figure

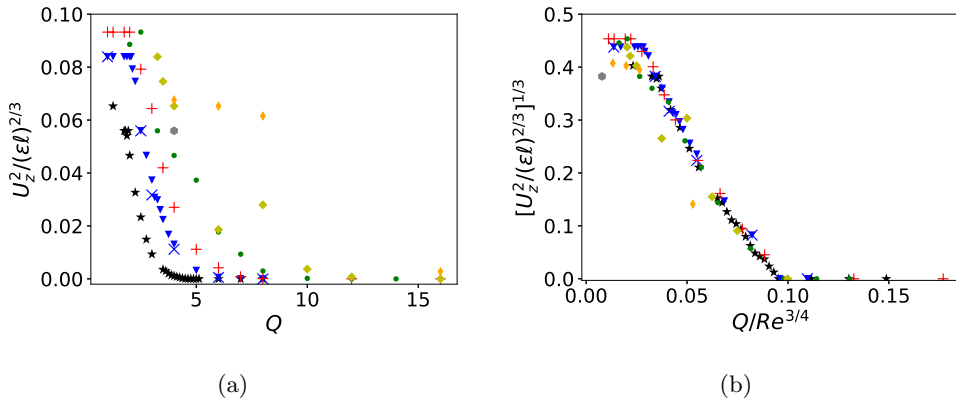


Figure 9: Left panel: U_z^2 as defined in equation (2.9) as a function of Q . Right panel: The various curves collapse when the abscissa is chosen to be η/H and the coordinate to be $U_{3D}^2/(\epsilon H)^{2/3}$. Raising the coordinate to the $1/3$ power, the curve becomes linear close to onset. This indicates that close to onset, U_v^2 scales approximately as $U_z^2 \approx (Q_c - Q)^3$, where $Q_c \approx 0.09 - 0.1 \approx Q_{2D}$. We note that the scaling exponent is different from that found for U_{3D}^2 .

8a), while in the right panel it is non-dimensionalised by $(\epsilon H)^{2/3}$ and raised to the power $1/2$ and plotted versus $\eta/H = Q/Re^{3/4}$. In figure 8a, it is shown that beyond some non-monotonic behaviour at small Q , the 3D energy decreases monotonically with Q until it reaches zero at Q_{2D} and remains zero beyond this point. The 3D energy is larger for larger Re at a given Q . The rescaling in figure 8b makes the various curves collapse nicely. In particular, the point where the energy vanishes is seen to be sharp and the same for all Re , namely at $\eta/H \approx 0.1$. Comparing with figure 6b, one sees that this point and Q_{2D} coincide within the range of uncertainties. This means that beyond Q_{2D} , not only is the equilibrium value of U_{is}^2 independent of Q , but also the 3D energy vanishes. This confirms that Q_{2D} corresponds to the point at which the motion becomes invariant along z .

Finally, figure 9 shows the vertical kinetic energy, non-dimensionalised by $(\epsilon l)^{2/3}$, once plotted versus Q and once taken to the $1/3$ power and plotted versus $Q/Re^{3/4}$. The general features of figure 9a are similar to figure 8a: like 3D energy, vertical kinetic energy decreases with Q until it reaches zero and it increases with Re . The curves collapse in figure 9b and the behaviour close to Q_{2D} becomes linear if the coordinate is raised to the $1/3$ power, indicating an approximate scaling $U_z^2 \approx (Q_c - Q)^3$ with $Q_c \approx Q_{2D}$. This indicates that the point beyond which the vertical kinetic energy vanishes is close to Q_{2D} , implying that beyond Q_{3D} , the motion is not only invariant along z but also restricted to the x-y plane. Hence, for $Q > Q_{2D}$, the flow has two-dimensionalised exactly.

4. Behaviour close to the transitions: hysteresis and intermittency

In this section, we discuss the behaviour close to the two transition points Q_{2D} and Q_{3D} . Each transition shows a different non-trivial behaviour. Close to Q_{3D} , we observe discontinuous transitions and hysteresis for some range of parameters, while close to Q_{2D} , we find both spatial and temporal intermittency with localised bursts of 3D energy.

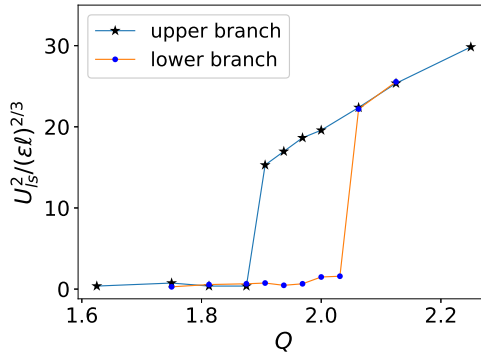


Figure 10: Hysteresis curve of large-scale kinetic energy (non-dimensionalised by the forcing energy). Two experiments are shown, first the ‘lower branch’ starting from small Q (deep layer) and increasing Q and the ‘upper branch’ starting from large Q (thin layer) and decreasing Q .

4.1. Close to Q_{3D} : Discontinuity and Hysteresis

We begin by discussing the behaviour of the flow for Q close to Q_{3D} where a sharp increase of the large-scale energy was observed. This sharp increase could indicate the presence of a discontinuity that could further imply the presence of hysteresis. To verify the presence of a discontinuity we need perform many different runs varying Q in small steps as well as verifying sensitivity to initial conditions. To do this, a hysteresis experiment has been performed at $Re = 406$, consisting of two series of runs, that we will refer as the ‘upper branch’ and the ‘lower branch’. On the upper branch, we started with random initial conditions and $Q \approx 2.25$ for which the system reaches a condensate equilibrium with an associated non-zero value of large-scale energy. Once the run has equilibrated, we use that equilibrium state to initialise a run at $Q \rightarrow Q - \Delta Q$ with $\Delta Q = 0.1$. By decreasing Q , the physical height of the box is increased. To be able to use the equilibrium state reached at one Q as initial condition for a neighbouring Q , the z -dependence of the velocity field is scaled and the velocity field is projected onto its divergence-free part, formally $v(x, y, z) \rightarrow \mathbb{P}v(x, y, \lambda z)$, where $\mathbb{P} = \mathbb{I} - \nabla^{-2} \nabla(\nabla \cdot)$. Having changed Q and applied this procedure, we let the system equilibrate to a new condensate state. This is repeated five more times (step size reduced to $\Delta Q = 0.05$ and then $\Delta Q = 0.025$) down to $Q \approx 1.9$. When Q is now lowered 0.025 further, the condensate decays into three-dimensional turbulence and the large-scale energy saturates to close to zero. Reducing Q even more, the large-scale energy remains small, indicating a three-dimensional turbulent state. The lower branch was calculated similarly, with the only difference that the experiment started at low Q and Q was increased in steps of 0.05 and then of 0.025. For small Q , the two branches coincide, while the lower branch remains at low large-scale energies (3D turbulence) up to $Q \approx 2.025$. For Q larger than $Q = 2.025$, the lower branch merges with the upper branch, closing the hysteresis loop and a condensate is spontaneously formed from three-dimensional turbulence. In other words, for $Re = 406$ in the range $1.9 \leq Q \leq 2.025$, there are multiple steady states and to which state the system will saturate depends on the initial conditions. The flow for two such states starting from different initial conditions for $Q \approx 1.97$ are visualized in 11.

The following remarks are in order: although for each Q we ran the simulations until a

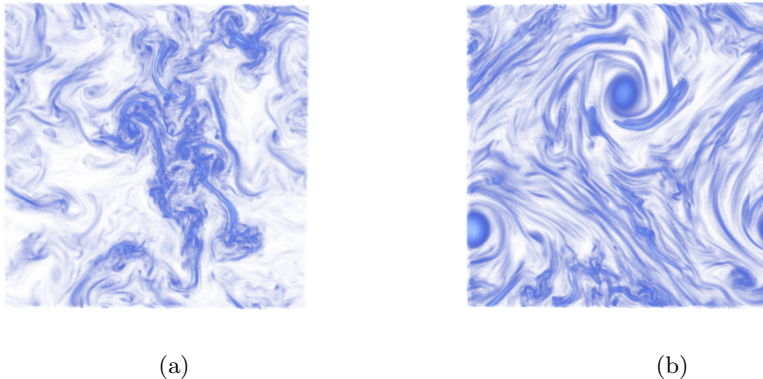


Figure 11: Figures 11a and 11b visualise the typical flow field after long simulation time at $Q \approx 1.97$ in the hysteresis experiment on the upper (11b) and lower (11a) branches. The lower branch flow field is characterised by small scale structures and the absence of large-scale organisation, reminiscent of three-dimensional turbulence. By contrast, the upper branch flow field shows the formation of two large-scale vortices in addition to a fair amount of small scale-structures in between them.

clear saturation was achieved, since we are dealing with a noisy system, rare transitions can exist between the two branches of the hysteresis loop. To test this, we picked the point $Q \approx 1.97$ on both lower and upper branches and ran them for a long time (thousands of eddy turnover times $\tau = (L^3/\epsilon)^{1/2}$). In neither run did we see a transition between the two branches, indicating that such transitions are rare (if not absent) in the middle of the hysteresis loop. Near the edges of the hysteresis loop at $Q \approx 2.05$ and $Q \approx 1.9$, the dependence on simulation time is likely to be stronger, but this has not been investigated.

Furthermore, we note that the bifurcation diagram of figure 10 corresponds to a relatively low Reynolds number $Re = 406$. Whether this subcritical behaviour persists at larger Re and/or larger box sizes (smaller K) is still an open question. Figure 7 suggests that a at $Q = Q_{3D}$ discontinuity continues to exist up to high Reynolds numbers ($Re = 2031$ shown there). In addition, we found more points at higher Reynolds numbers that showed a dependence on initial conditions but without having enough values of Q to create a hysteresis diagram. These findings suggest that subcritical behaviour and hysteresis might survive even at high Reynolds numbers. However, due to the high computational cost at higher resolution and the long duration of the runs required to verify that the system stays in a particular state, we could not investigate this possibility in detail. Further simulations at larger Re and possibly smaller K (larger boxes) are required to resolve this issue.

The hysteretic behaviour described above is likely due to the stability properties of the vortices making up the condensate. Once they are formed, the vortices are able to resist 3D perturbations by shearing them out. Similar hysteretic behaviour has recently been reported in rotating turbulence, see (Yokoyama & Takaoka 2017). More generally, multistability is observed in many turbulent flows, see (Weeks *et al.* 1997; Ravelet *et al.* 2004) as examples.

4.2. Close to Q_{2D} : Intermittent bursts

Next, we discuss the behaviour of the flow close to the second critical point Q_{2D} . A typical time series of 3D energy for $Q \lesssim Q_{2D}$ is shown in figure 12a. One observes bursty

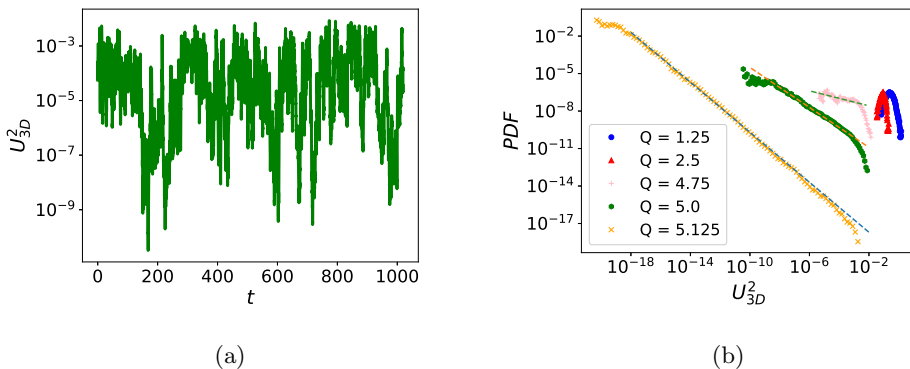


Figure 12: Plots showing temporal intermittency for $Re = 203$. Figure 12a shows a typical time series (y-axis is logarithmic) of 3D energy close to Q_2 . Specifically, here $Q = 5$, where $Q_{2D} \approx 5.13$ for this Reynolds number. Figure 12b shows PDF corresponding to this time series as well as for different values of Q (PDFs shifted by a constant factor to improve visibility). The four different symbols mark different values of Q , while the dotted lines correspond to a power law with exponent -1 (lower dotted line), -0.8 (middle dotted line) and -0.3 (upper dotted line) respectively.

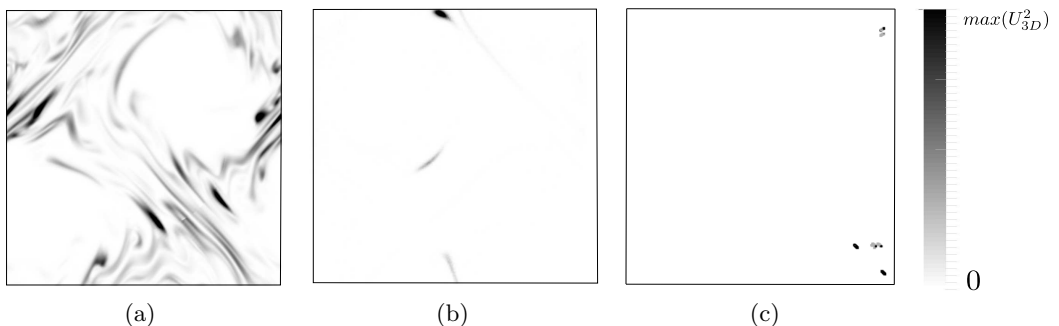


Figure 13: Snapshots of the 3D energy density for $Re = 203$ and $Q = 2.5$ (figure 13a), $Q = 5.0$ (figure 13b) and $Q = 5.125$ (figure 13c), (corresponding to figure 12). The colorbar shown on the right is chosen in each plot such that the maximum value of 3D energy is shown in black. As Q increases towards $Q_{2D} \approx 5.13$, U_{3D}^2 becomes more and more localised. In figure 13c, the 3D energy is concentrated in small columnar structures (upper and lower right-hand corner) which are absent in figure 14c.

behaviour and variations over many orders of magnitude, indicating on-off intermittency (Fujisaka & Yamada 1985; Platt *et al.* 1993). On-off intermittency refers to the situation where a marginally stable attractor loses or gains stability due to noise fluctuations. When instability is present, a temporary burst is produced before the system returns to the attractor. The on-off intermittency predicts that the unstable mode X follows a power-law distribution $P(X) \propto X^{\delta-1}$ for $X \ll 1$ where δ measures the deviation from onset (here $\delta \propto (Q_{2D} - Q)/Q_{2D}$) and all moments scale linearly with the deviation $\langle X^n \rangle \propto \delta$.

In our system, the 2D flow forms the marginally stable attractor that loses stability to 3D perturbations depending on the exact realisation of the 2D turbulent flow. To formulate this, we decompose the velocity field into its 2D and 3D parts, $\mathbf{u} = \mathbf{u}_{2D} + \mathbf{u}_{3D}$,

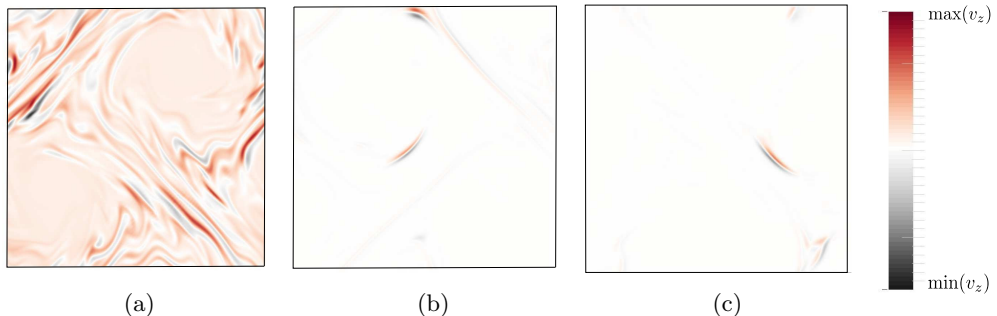


Figure 14: Snapshots of the vertical velocity field for $Re = 203$ and $Q = 2.0$ (figure 14a), $Q = 5.0$ (figure 14b) and $Q = 5.125$ (figure 14c). The colour scale on the right is rescaled in each plot such that the minimum (negative) is shown in black and the maximum (positive) in red. (same as in figure 12). As in figure 13, u_z becomes localised in smaller and smaller areas as Q increases, i.e. there is increasing spatial intermittency as $Q_{2D} \approx 5.13$ is approached.

where the 2D part is defined as the Fourier sum of \mathbf{u} restricted to modes with $k_z = 0$. Filtering the 3D component of equation (2.1), dotting with \mathbf{u}_{3D} and integrating over the domain gives

$$\partial_t U_{3D}^2 = - \langle \{\mathbf{u}_{3D} \cdot \nabla \mathbf{u}_{2D}\} \cdot \mathbf{u}_{3D} \rangle - \nu \langle |\nabla \mathbf{u}_{3D}|^2 \rangle, \quad (4.1)$$

where $\langle \cdot \rangle$ denotes integration over the domain. The chaotic 2D motions then act as multiplicative noise while the viscous terms provide a mean decay rate.

Figure 12 shows that temporal intermittency is present in the thin-layer system. Panel (a) shows a typical time series of 3D energy at $Q \lesssim Q_{2D}$ which fluctuates over six orders of magnitude. In particular, as mentioned before, there are burst-like excursions in 3D energy. In figure 12b, PDFs constructed from this time series and similar ones for different values of Q are shown along with dotted lines that indicate power laws with exponents close to -1 , -0.8 and -0.3 . The PDFs are very close to a power law for a significant range of U_{3D}^2 and the exponent converges to minus one as the transition is approached, in agreement with on-off intermittency predictions. However, the scaling of 3D energy with deviation from onset shown in figure 8b deviates from the linear prediction of on-off intermittency, but is approximately $\langle U_{3D}^2 \rangle \propto (Q_{2D} - Q)^2$. For U_z^2 , figure 9 seems to suggest yet a different scaling, namely $\langle U_z^2 \rangle \propto (Q_{2D} - Q)^3$. A similar behaviour was also found in (Benavides & Alexakis 2017) and was attributed to the spatio-temporal character of the intermittency that not only leads to 3D modes appearing more rarely in time as criticality is approached but to also occupy a smaller fraction of the available volume. This appears also to be the case in our results as demonstrated in figures 13 and 14 where U_{3D}^2 and the vertical component u_z of the velocity are plotted for three different values of Q . As Q approaches the critical value Q_{2D} , the structures become smaller for U_{3D}^2 and u_z with the difference that U_{3D}^2 shows spot-like structures in figure 13c which are absent for u_z . This difference may be related to the two different scalings observed for U_{3D}^2 and U_z^2 with $Q_c - Q$ small: if the volume fraction of vertical motion depends on $Q_c - Q$ to a different power than that of vertical variations, the two different behaviours of U_z^2 and U_{3D}^2 would follow. A more detailed quantitative investigation of the scaling of volume fraction will be needed to clarify this.

In summary, we have found nontrivial behaviour close to both transitions: we have observed hysteresis near Q_{3D} and spatio-temporal intermittency close to Q_{2D} where the

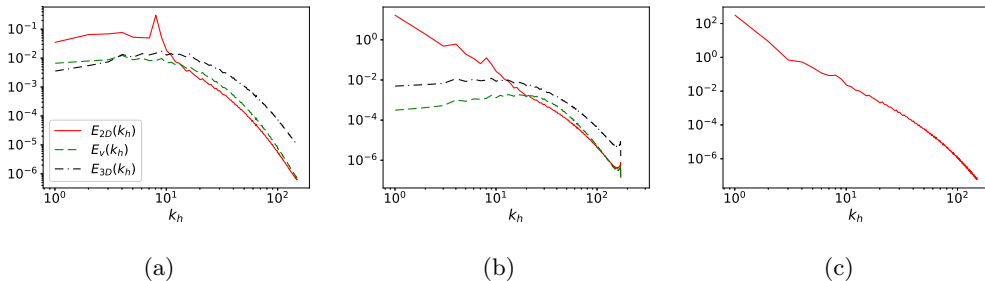


Figure 15: Three different energy spectra, $E_{2D}(k_h)$, $E_z(k_h)$, $E_{3D}(k_h)$ are shown at $Re = 609$ for 3D turbulence (figure 16a), 2D turbulence (figure 15c) and an intermediate value of $Q \in (Q_{3D}, Q_{2D})$ (figure 15b) called flux-loop condensate, see main text. For 3D turbulence ($Q = 1.25 < Q_{3D}$), the peak of the energy spectrum is at the forcing scale and 2D energy is about one order of magnitude larger than the other two components. In the flux-loop condensate ($Q = 4$), there is a maximum in the 2D energy at large scales but the 3D and vertical energy are non-zero. In the 2D turbulence case ($Q = 16 > Q_{2D}$), there is a maximum in 2D energy at the large scales while 3D and vertical energy are vanishingly small.

temporal behaviour seems to be described by on-off intermittency. Taking into account these effects will be crucial to understand the exact nature of the observed transitions. Nonetheless, the simple model presented in the section 6 will be shown to predict many correct characteristics close to Q_{2D} .

5. Spectra and fluxes

In this section, we discuss the spectral space properties of the three different regimes described in the previous section. Figure 15 shows the energy spectra $E_h(k_h)$, $E_z(k_h)$ and $E_{3D}(k_h)$ for a flow in which there is no inverse cascade in panel (a), for a flow where a condensate is formed but the the 3D part of the flow is still active in panel (b) and $E_h(k_h)$ for a flow that has become 2D in panel (c). In the first case, where $Q < Q_{3D}$ all three spectra are of the same order, with a small excess of $E_h(k_h)$ in the large scales and an excess of $E_{3D}(k_h)$ in the small scales. This is the 3D turbulent case. The small scale separation between the forcing and the dissipation scale does not allow us to observe a $k^{-5/3}$ power-law regime. In the middle panel, $E_h(k_h)$ clearly dominates in the large scales, forming a steep spectrum (close to $E_h(k_h) \propto k_h^{-4}$). However, at wavenumbers larger than the forcing wavenumber $k_f = 8$, $E_z(k_h)$ and $E_{3D}(k_h)$ become of the same order as $E_h(k_h)$. In the right panel, where $Q > Q_{2D}$, the spectra $E_z(k_h)$ and $E_{3D}(k_h)$ have reduced to values close to the round-off error and are not plotted. The 2D spectrum $E_h(k_h)$ displays again a steep power-law behaviour close to $E_h(k_h) \propto k_h^{-4}$.

Figure 16 shows the energy fluxes as defined in eqs. (2.11-2.13) for the same three cases that were examined in figure 15. In panel (a), where the case $Q < Q_{3D}$ is examined, there is almost no inverse flux of energy and $\Pi(k_h)$ is practically zero. The small inverse flux that is observed for $\Pi_{2D}(k_h)$ at $k < k_f$ does not reach the largest scale of the system and is nearly completely balanced by $\Pi_{3D}(k_h)$, which is forward. At wavenumbers larger than k_f , the total flux is positive and is completely dominated by Π_{3D} . This is to be contrasted with the rightmost panel (c) with $Q > Q_{2D}$, where at small wavenumbers, the flux is negative and is dominated by the 2D flow, while at large wavenumbers there is a very small forward flux. For the intermediate case shown in panel (b), for which

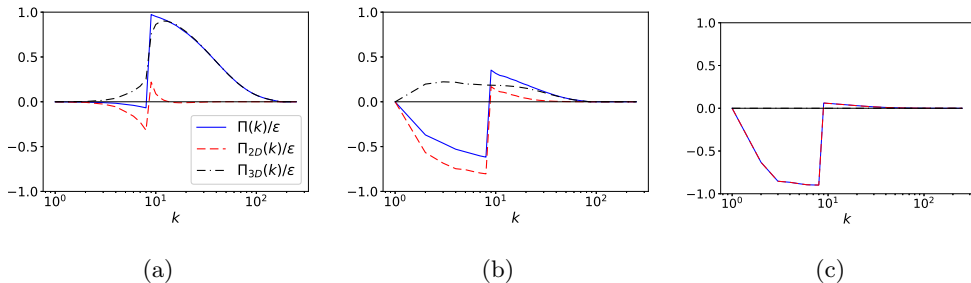


Figure 16: Three different components of spectral energy flux, $\Pi(k_h)$, $\Pi_{2D}(k_h)$ and $\Pi_{3D}(k_h)$, are shown for the same three cases and in the same order as in figure 15.

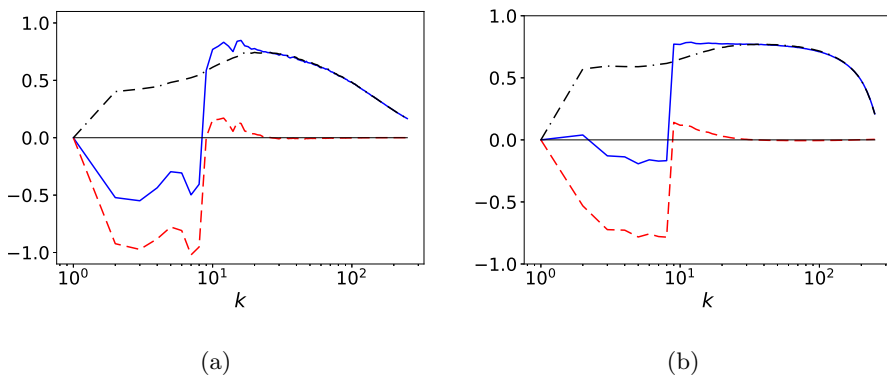


Figure 17: Flux loop condensate steady state fluxes for $Re = 4062$ in panel (a) and the hyper-viscous run in panel (b).

$Q_{3D} < Q < Q_{2D}$, there is an inverse energy flux. This flux can be decomposed into the 2D part $\Pi_{2D}(k_h)$ that is negative and the 3D part $\Pi_{3D}(k_h)$ that is positive. In other words, the 2D motions of the flow bring energy to the largest scales of the system which is then brought back to the small scales by the 3D motions of the flow which are associated with a forward energy flux, thus forming a loop for the energy transfer. For this reason, we refer to this case as *flux-loop condensate*.

Due to finite viscosity, part of the energy that arrives at the largest scale (shown in figure 16b) is dissipated. Therefore, the two fluxes are not completely in balance. As Re is increased, however, the fraction of the energy that is dissipated in the large scales is decreased and the two opposite fluxes come closer to balancing each other. This is shown in figure 17, where the energy fluxes for the highest Re simulation and for the simulation with hyper viscosity are plotted. The two opposite directed fluxes are closer in amplitude. At $Re \rightarrow \infty$ it is thus expected that the inverse and forward fluxes at large scales will be in perfect balance and all the energy is dissipated in the small scales. It is worth noting, however, that the inverse cascade (negative flux) due to the 2D components has much stronger fluctuations than the forward cascading flux that has led to the non-monotonic behaviour of the flux observed at small k due to insufficient time averaging.

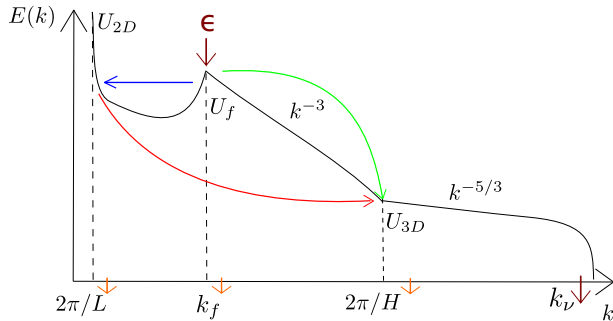


Figure 18: Sketch of three-mode model. The solid curve shows a hypothetical energy spectrum $E(k)$ of the condensate state. By definition of the condensate, $E(k)$ has a maximum of amplitude U_{2D}^2 at the scale of the system size $k = 2\pi/L$. Beyond the forcing scale $k_f = 2\pi/\ell$, where $E(k) \approx U_f^2$, there would be two-dimensional turbulence with $E(k) \propto k^{-3}$ until the the scale of the motion is comparable to the height of the box $k = 2\pi/H$, where $E(k) \approx U_{3D}^2$. Below this, one expects a spectrum close to three-dimensional turbulence with $E(k) \propto k^{-5/3}$. The energy injected at the forcing scale at a rate ϵ is transferred partly to large and partly to small scales as illustrated by the two arrows emanating from there. Next, there is another arrow indicating energy transfer from the large scales to the small scales. Finally, the short arrows next to $2\pi/L$, k_f and $2\pi/H$ represent the viscous dissipation happening at these scales due to the finiteness of Re and the arrow next to k_ν , the dissipation scale, indicates transfer of energy to the dissipation range.

6. A three-scale model

In this section, we formulate and analyse a simple three-mode ODE model which reproduces certain features of the DNS results described in section 3.

6.1. The general formulation

As illustrated in figure 18, we choose to formulate our model in terms of a 2D mode U_{2D} at the scale L of the domain, a mode U_f at the forcing scale ℓ and a 3D mode U_{3D} mode at the scale of the layer height H , whose interactions are spectrally non-local. The model describes the system at steady state where these scales are well separated, but it is not expected to capture the transient case where, due to the inverse cascade, all intermediate scales between L and ℓ participate. As in the previous sections, we will define $Q = \ell/H$, $K = \ell/L$ and $Re = (\epsilon\ell^4)^{1/3}/\nu$. The interactions between the modes are modelled using the concept of eddy viscosity, (see Kraichnan 1976), which amounts to modifying the molecular viscosity ν by additional terms involving the small-scale velocities that model the effect of small scales on the large scales as diffusive. It has been estimated in various limits in both in two and three dimensions (Yakhot & Sivashinsky 1987; Gama *et al.* 1994; Dubrulle & Frisch 1991; Meshalkin 1962; Sivashinsky & Yakhot 1985; Cameron *et al.* 2016; Alexakis 2018).

There are two notable limits where the dependence of eddy viscosity ν_E on the flow amplitude U_s and length scale l_s can be deduced. For $Re \rightarrow \infty$, one expects that ν_E becomes independent of ν and the only dimensional possibility for ν_E is given by

$$\nu_E = c_1 U_s l_s. \quad (6.1)$$

where c_1 is a non-dimensional number. In the low- Re limit, however, this scaling does

not hold. In this case, an asymptotic expansion can be carried out (Dubrulle & Frisch 1991) which reveals that

$$\nu_E = c_2 \frac{U_s^2 \ell_s^2}{\nu} + O(U_s^4 \ell_s^4 / \nu^2), \quad (6.2)$$

where the non-dimensional number c_2 can be evaluated by the expansion. The sign of the coefficients c_1, c_2 depends on the exact form of the small scale flow and in particular its dimensionality. Two-dimensional flows are expected to have a negative eddy viscosity and transfer energy to the large scales, while 3D flows are thought to have positive eddy viscosity and transfer energy to the small scales.

For our model, we are going to consider that interactions among the three different scales $L > \ell > H$ are such that the flow at the smaller scale acts as an eddy viscosity on the flow at the larger scale. These interactions are illustrated in figure 18. In particular, the energy injected at a constant rate ϵ at the forcing scale is transferred partly to the large scale L (via a negative eddy viscosity $-\mu$) and partly to the small scales (via a positive eddy viscosity σ). The large scales in turn may lose energy directly to the small scales (via a positive eddy viscosity term η). The small scales may dissipate energy by transferring it to the dissipation range, which is modelled via a non-linear energy sink. In addition, the Reynolds number at all scales is finite, so that all scales may lose energy via dissipation. The set of equations below formalises these ideas:

$$\frac{d}{dt} U_{2D}^2 = -(\nu - \mu + \eta) \frac{U_{2D}^2}{L^2}, \quad (6.3a)$$

$$\frac{d}{dt} U_f^2 = \epsilon - (\nu + \sigma) \frac{U_f^2}{\ell^2} - \mu \frac{U_{2D}^2}{L^2}, \quad (6.3b)$$

$$\frac{d}{dt} U_{3D}^2 = \eta \frac{U_{2D}^2}{L^2} + \sigma \frac{U_f^2}{\ell^2} - \frac{U_{3D}^3}{H} - \nu \frac{U_{3D}^2}{H^2}, \quad (6.3c)$$

Note in particular that eddy viscosities do not dissipate energy, but merely redistribute energy between different scales. Adding the three model equations leads to

$$\frac{d}{dt} (U_{2D}^2 + U_f^2 + U_{3D}^2) = \epsilon - \nu \left(\frac{U_{2D}^2}{L^2} + \frac{U_f^2}{\ell^2} + \frac{U_{3D}^2}{H^2} \right) - \frac{U_{3D}^3}{H},$$

showing that the total kinetic energy only changes due to molecular viscosity ν , the energy injection ϵ and the sink term representing the 3D energy cascade to the dissipation range, U_{3D}^3/H . Depending on Re , either of the two expressions for eddy viscosity (eqs. 6.1, 6.2) may be expected to yield an adequate description of the multi-scale interactions in the problem. A model that interpolates smoothly between the large and small Re limits is given by

$$\mu = \alpha \frac{U_f^2 \ell^2}{\nu + U_f \ell}, \quad \eta = \beta \frac{U_{3D}^2 H^2}{\nu + U_{3D} H}, \quad \sigma = \gamma \frac{U_{3D}^2 H^2}{\nu + U_{3D} H}, \quad (6.4)$$

where α, β, γ are positive non-dimensional coupling constants. In the large and small Re limits, the above expressions converge to the parametrisations for the eddy viscosities described before. Depending on the parameters, this nonlinear dynamical system possesses a varying number of fixed points. To classify them, first note that for $\epsilon \neq 0$, U_f must be non-zero at any fixed point by (6.3b) and the definition of μ in (6.4). Hence there are four possibilities:

- (a) *laminar state*: $U_{2D} = U_{3D} = 0$ (all energy in forcing scale flow),
- (b) *3D turbulence state*: $U_{2D} = 0$ and $U_{3D} \neq 0$,
- (c) *2D condensate state*: $U_{2D} \neq 0$ and $U_{3D} = 0$ and

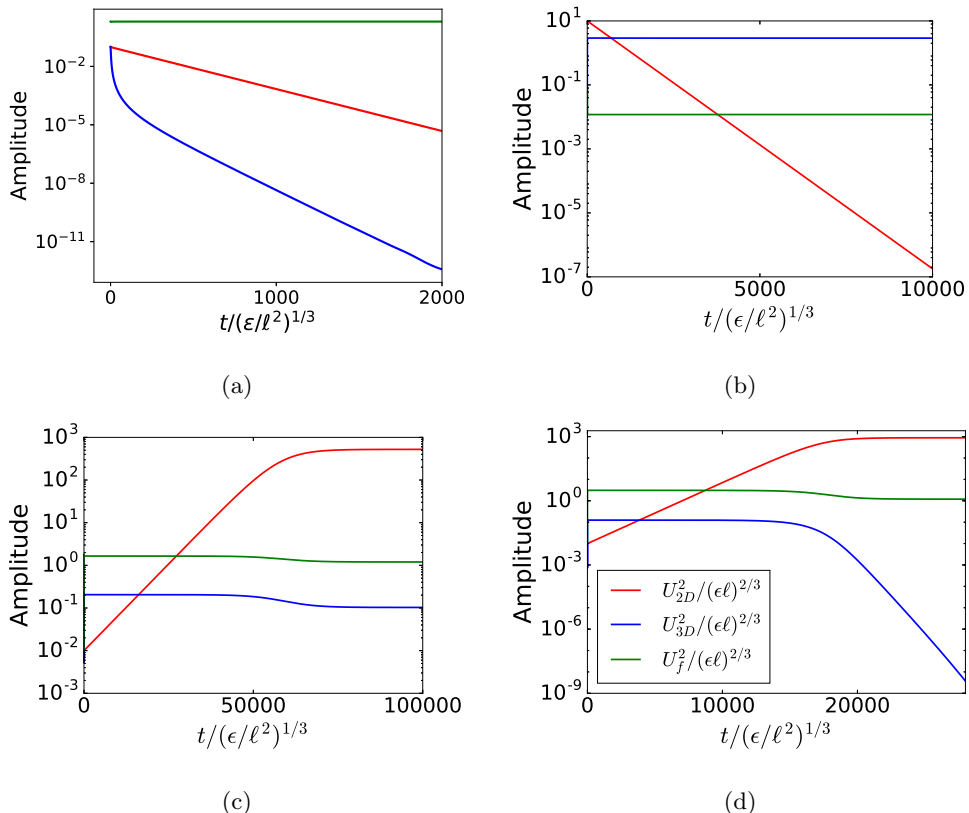


Figure 19: Typical time-series of the full three-scale model in the 3D turbulence (19b), split-cascade (19c), 2D-turbulent (19d) and laminar (19a) regimes. Only Q is different between figures 19b ($Q = 0.2$), 19c ($Q = 4.5$) and 19d ($Q = 5.887$), all other parameters are identical ($Re = 10$, $\alpha = 0.1$, $\beta = 0.01$, $\gamma = 10$, $K = \ell/L = 0.1$). The parameters for figure 19a are $Re = 2$, $\alpha = 0.001$, $\beta = 10$, $\gamma = 10$, $K = \ell/L = 0.1$ and $Q = 1.6405$.

(d) *flux-loop condensate* state: $U_{2D} \neq 0$ and $U_{3D} \neq 0$.

The laminar state appears for values of Re below a critical value Re_c and there is no transfer, neither to large nor to small scales. Above this critical value, one of the three other states is stable, depending on the value of $Q = \ell/H$, which we will consider here as our control parameter. For small values of Q (large H), the system is in the 3D turbulence state, where energy is only exchanged between the forcing scale ℓ and the scale of the layer height. Above the critical value of Q_{3D} , the system transitions to the flux-loop condensate state where part of the injected energy is transferred to the large scales and then back to the small scales, thus forming a loop. Finally, at sufficiently large Q above a second critical point Q_{3D} , the system transitions to the 2D condensate where it follows 2D dynamics and there is only a transfer of the injected energy to the large scales. The time evolution of the three energies for these four different states is shown in fig. 19.

For simplicity, to be able to evaluate analytically the critical points Re_c , Q_{2D} and Q_{3D} in this model, it is useful to consider explicitly the two limits $Re \rightarrow 0$ and $Re \rightarrow \infty$ of equations (6.3) and (6.4).

6.2. Low Re limit

In the low Re limit, the different eddy viscosities take the form of equation (6.2). Thus, the model equations become

$$\partial_t U_{2D}^2 = - \left(\nu - \alpha \frac{U_f^2 \ell^2}{\nu} + \beta \frac{U_{3D}^2 H^2}{\nu} \right) \frac{U_{2D}^2}{L^2}, \quad (6.5a)$$

$$\partial_t U_f^2 = \epsilon - \left(\nu + \gamma \frac{U_{3D}^2 H^2}{\nu} \right) \frac{U_f^2}{\ell^2} - \alpha \frac{U_f^2 \ell^2}{\nu} \frac{U_{2D}^2}{L^2}, \quad (6.5b)$$

$$\partial_t U_{3D}^2 = \beta \frac{U_{3D}^2 H^2}{\nu} \frac{U_{2D}^2}{L^2} + \gamma \frac{U_{3D}^2 H^2}{\nu} \frac{U_f^2}{\ell^2} - \frac{U_{3D}^3}{H} - \nu \frac{U_{3D}^2}{H^2}. \quad (6.5c)$$

To obtain this limiting form of the equations, it is assumed that $\nu \gg U_f \ell, U_{3D} H$. The laminar flow is unstable to 3D perturbations when $Q < \gamma^{1/4} Re^{3/4}$ and unstable to 2D perturbations when

$$Re > 1/\alpha^{1/3}. \quad (6.6)$$

When the latter condition is satisfied and H is sufficiently small (Q sufficiently large), the system is attracted to the 2D condensate state, given by

$$U_{2D}^2 = \frac{L^2}{\nu} \left(\epsilon - \frac{\nu^3}{\ell^4 \alpha} \right), \quad U_f^2 = \frac{\nu^2}{\alpha \ell^2}, \quad U_{3D} = 0.$$

Note that U_{2D}^2 is inversely proportional to the viscosity and proportional to L^2 in agreement with the scaling of the data in figure 6b. The 2D condensate state ceases to be an attractor of the system when H is sufficiently large such that U_{3D} becomes unstable. This occurs when

$$H^4 > \left(\epsilon \frac{\beta}{\nu^3} + \frac{\gamma - \beta}{\alpha \ell^4} \right)^{-1}. \quad (6.7)$$

Hence, we conclude that

$$Q_{2D} = \left(\epsilon \frac{\beta}{\ell \nu^3} + \frac{\gamma - \beta}{\alpha \ell^5} \right)^{1/4} = \left(\beta Re^3 + \frac{\gamma - \beta}{\alpha} \right)^{1/4}. \quad (6.8)$$

Thus, for moderate values of Re , there is an approximate scaling $Q_{2D} \propto Re^{3/4} \propto \eta$. (Note that $Re^3 > 1/\alpha$ due to eq. (6.6).) The dissipation length in agreement with the results obtained in section 3, where we were able to collapse the U_{2D} data points by rescaling such that $Q Re^{3/4} = \eta/H$ is on the abscissa and $U_{2D}^2 K^2 / [Re(\epsilon \ell)^{2/3}]$ on the coordinate. Results from the full model equations (6.3) and (6.4) are shown in figure 20 where the same scaling is applied. The corresponding plots for equations (6.5) are very similar. Furthermore, an asymptotic analysis close to Q_{2D} described in the appendix reveals that the scaling for $U_{3D}^2 \propto (Q_{2D} - Q)^2$ which is the same as in the DNS results shown in figure 8b although no intermittency is present. The other critical point Q_{3D} , where the 3D turbulence solution changes stability, can be evaluated numerically and is found to increase with Re indefinitely. This, however, is an artefact of the low Re asymptotic form of the eddy viscosities used in this subsection.

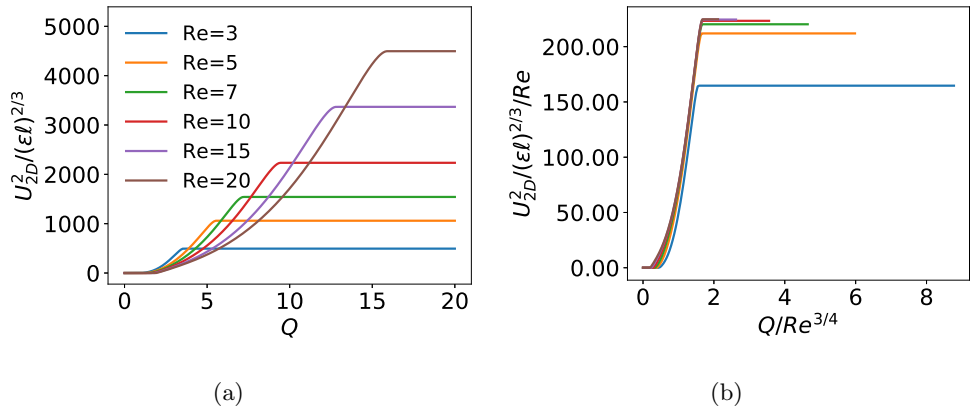


Figure 20: Bifurcation diagram in terms of $U_{2D}^2/(\epsilon\ell)^{2/3}$ for the full model equations (6.3) and (6.4) with and without rescaling. The overall structure of the plots is strongly reminiscent of corresponding DNS results in figures 6a and 6b. In figure 20a, U_{2D} vanishes at small Q (3D turbulence), increases monotonically between the critical points Q_{3D} and Q_{2D} and remains constant for $Q > Q_{2D}$. Figure 20b shows the same data as 20a, but with the abscissa rescaled by $Re^{3/4}$ and the coordinate rescaled by Re as in figure 6b. The collapse becomes more accurate the higher Re . The parameters used are $\alpha = 0.51$, $\beta = 8$, $\gamma = 0.1$, $\ell = L/15 = 1$.

6.3. Infinite Re limit

In the infinite Re limit, the eddy viscosities given in equation (6.4), take the form (6.1) and the resulting system of equations reads

$$\partial_t U_{2D}^2 = \frac{(\alpha U_f \ell) U_{2D}^2}{L^2} - \frac{(\beta U_{3D} H) U_{2D}^2}{L^2} \quad (6.9a)$$

$$\partial_t U_f^2 = \epsilon - \frac{(\alpha U_f \ell) U_{2D}^2}{L^2} - \frac{(\gamma U_{3D} H) U_f^2}{\ell^2} \quad (6.9b)$$

$$\partial_t U_{3D}^2 = \frac{(\beta U_{3D} H) U_{2D}^2}{L^2} + \frac{(\gamma U_{3D} H) U_f^2}{\ell^2} - \frac{U_{3D}^3}{H} \quad (6.9c)$$

One can easily see that these equations do not permit a fixed point with $U_{3D} = 0$ when $\epsilon \neq 0$. To show this, first note that, as in the finite Re case, the forcing scale velocity U_f cannot vanish at a fixed point if $\epsilon \neq 0$. Assume there exists a fixed point with $U_{3D} = 0$. Then equation (6.9c) is trivially satisfied, while (6.9a) implies that $U_{2D} = 0$ or $U_f = 0$. Since U_f must be non-zero, we have $U_{2D} = 0$, which leads to a contradiction in equation (6.9b) for any $\epsilon \neq 0$. Hence neither a laminar flow state nor a 2D condensate state exists in the system in the infinite Re limit. The only two remaining fixed points are three-dimensional turbulence and the flux-loop condensate. The former is given by

$$U_{2D}^2 = 0, \quad U_f^2 = \frac{\epsilon^{2/3} \ell^2}{\gamma H^{4/3}}, \quad U_{3D}^2 = (\epsilon H)^{2/3} \quad (6.10)$$

Using this result and considering equation (6.9a), we can find that the 3D turbulence fixed point becomes unstable to 2D perturbations at

$$H = \left(\frac{\alpha^2}{\beta^2 \gamma} \right)^{1/4} \ell \quad (6.11)$$

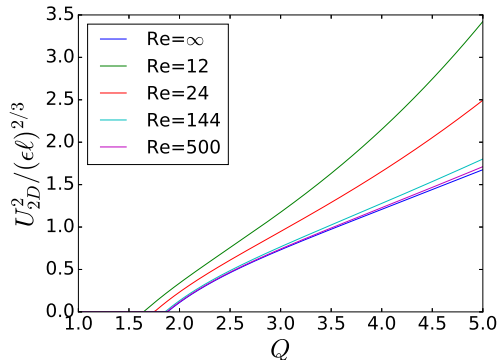


Figure 21: The stable branch of the U_{2D}^2 component (non-dimensionalised) of bifurcation diagram is shown for four different Reynolds numbers in the intermediate model as well as for the infinite Reynolds number model. The $Re = 500$ and the $Re = \infty$ cases are almost indistinguishable. The parameters used are $L = \ell = 1$, $\alpha = 1$, $\beta = 5$, $\gamma = 0.5$.

and thus we obtain that

$$Q_{3D} = \left(\frac{\beta^2 \gamma}{\alpha^2} \right)^{1/4}. \quad (6.12)$$

Hence, in the infinite Re limit of our three-scale model, there remains only one bifurcation, namely that at Q_{3D} between two-dimensional turbulence and the split cascade state. The second critical point Q_{2D} vanishes to infinity as $Q_{2D} \propto Re^{3/4}$ in this limit. Figure 21 demonstrates close to Q_{3D} that the full model converges to the solution obtained from the asymptotic form of the equations 6.9 as Re increases. This is consistent with the convergence observed in the DNS in figure 6b.

To conclude this section we mention that the present model is very successful in giving an overall description of the simulations by predicting both the location (up to scaling factor) of the critical points and the scaling of the energies as a function of Reynolds number. We note, however, that the model captures neither the sub-critical bifurcation observed in the simulations close to Q_{3D} , nor the intermittent behaviour close to Q_{2D} .

7. Conclusions

We have examined the steady state of thin-layer turbulence as a function of the system parameters using an extensive set of high-resolution numerical simulations.

It is shown that the split cascade observed at early times of the flow evolution (Celani *et al.* 2010; Benavides & Alexakis 2017; Musacchio & Boffetta 2017) leads to the formation of condensate states in the long-time limit. Three different states were found for large Re . (a) For very thick layers the system saturates in a regular 3D turbulence state with no inverse cascade and negligible dissipation at large scales. (b) At intermediate layer thickness, a flux-loop condensate is formed such that part of the energy transferred to the condensate by the 2D motions is transferred back to the small scales by the 3D motions. (c) For very thin layers, the system becomes two-dimensional and forms a 2D-turbulence condensate, where the energy that cascades inversely is balanced by the dissipation due to viscosity at large scales. The transition from 3D turbulence to the flux loop condensate occurs at a critical height H_{3D} (Q_{3D}) that is a decreasing (increasing) function of Re , but saturates at a Re independent value for large Re . For values of H slightly smaller

than H_{2D} the amplitude of the large-scale velocity U_{ls}^2 jumps discontinuously to a large value and increases linearly after that. Close to the threshold, a hysteresis diagram was constructed where the system saturates to a different attractor (3D turbulence or flux-loop condensate) depending on the initial conditions. Whether this hysteresis behaviour persists at larger Re and larger box-sizes $1/K$ remains an open question. The flux loop condensate transitions to a 2D turbulence condensate at a critical height H_{2D} that scales like $H_{2D} \propto \ell Re^{-3/4}$ unlike the early stages of the development that scaled like $H_{2D} \propto \ell Re^{-1/2}$ (Benavides & Alexakis 2017). For the 2D turbulence condensate, the large-scale energy was found to be inversely proportional to Re and independent from H . The transition from a flux loop-condensate to 2D turbulence condensate showed strong spatio-temporal intermittency leading to a scaling of the average 3D energy as the square of the deviation from onset $U_{3D}^2 \propto (H - H_{2D})^2$, similarly as in (Benavides & Alexakis 2017).

Most of the features above were captured by a three-scale eddy viscosity model that predicted correctly the scaling of the condensate energy with H and Re and location of the critical heights H_{3D}, H_{2D} , as well as their dependence on Re . However, the model failed to predict correctly the behaviour of the flow close to the two critical heights, i.e. no discontinuity was present in the model close to H_{3D} and no intermittency was found close to H_{3D} . The complexity of the physics involved that leads to the behaviour of the flow close to criticality goes beyond the simple phenomenology used to construct the present model and both critical heights deserve both further investigation by numerical simulations, experiments and theoretical models. Concerning the realisability of the present numerical results in an experiment, it needs to be stressed that this study only considers the triply periodic domain for simplicity. When attempting to transfer the results to non-slip boundary conditions, a word of caution is therefore in order: viscous boundary layers may lead to large-scale drag, which is explicitly left out from the model set-up used here. However, in a carefully designed experiment, the transition to the thin-layer turbulent condensate might still be observed. Such an experiment would be extremely valuable for a better understanding of turbulent condensates in thin layers since it would allow higher Reynolds numbers provide better statistics.

Acknowledgements

This work was granted access to the HPC resources of MesoPSL financed by the Région Ile de France and the project Equip@Meso (reference ANR-10-EQPX-29-01) of the programme Investissements d’Avenir supervised by the Agence Nationale pour la Recherche and the HPC resources of GENCI-TGCC-CURIE & CINES Occigen (Project No. A0010506421 & A0030506421) where the present numerical simulations have been performed. This work has also been supported by the Agence nationale de la recherche (ANR DYSTURB project No. ANR-17-CE30-0004). AvK was supported by Deutscher Akademischer Austauschdienst and Studienstiftung des deutschen Volkes.

Appendix A. Derivation of near-threshold behaviour of three-scale model

Here, we derive the behaviour close to H_2 and H_3 in the three-scale model. First consider $H = H_2(1 + \delta)$ and let $\mathbf{x} = (x, y, z)^T = (U_{2D}^2, U_{3D}^2, V_{2D}^2)^T$, $\tilde{\mathbf{x}} = (\tilde{x}, \tilde{y}, \tilde{z})^T = \mathbf{x} - (x_2, y_2, 0)^T$, where $x_2 = (U_{2D}^{(2)})^2$ and $y_2 = (U_f^{(2)})^2$. Then equations (6.5) can be

rewritten exactly in the form

$$\frac{d}{dt} \tilde{\mathbf{x}} = \begin{pmatrix} -\frac{\nu}{L^2} & \frac{\alpha \ell^2 x_2}{\nu L^2} & -\frac{\beta x_2 H^2}{\nu L^2} \\ -\frac{\alpha y_2}{\nu L^2} & -\frac{\nu}{\ell^2} & -\frac{\gamma H^2 y_2}{\nu \ell^2} \\ 0 & 0 & C \end{pmatrix} \tilde{\mathbf{x}} + \begin{pmatrix} 0 \\ 0 \\ -1/H_2 \end{pmatrix} \tilde{z}^{3/2} + \tilde{\mathbf{x}}^T \mathbf{B} \tilde{\mathbf{x}}, \quad (\text{A } 1)$$

where $C = -\frac{\nu}{H^2} + \frac{\beta H^2 x_2}{\nu L^2} + \frac{\gamma H^2 y_2}{\nu \ell^2}$ and the specific coefficients of the quadratic term are irrelevant here. By definition of H_2 , $C(\delta = 0) = -\frac{\nu}{H_2^2} + \frac{\beta H_2^2 x_2}{\nu L^2} + \frac{\gamma H_2^2 y_2}{\nu \ell^2} = 0$. Hence, for small δ , $C \propto \delta$. Specifically,

$$C \stackrel{\delta \ll 1}{\approx} \left(\frac{2\nu}{H_2^2} + \frac{2\beta x_2}{\nu L^2} + \frac{2\gamma y_2}{\nu \ell^2} \right) \delta. \quad (\text{A } 2)$$

Hence, considering the \tilde{z} component and balancing the linear term with the $\tilde{z}^{3/2}$ term, we deduce that

$$\tilde{z} \stackrel{\delta \ll 1}{\approx} \left(\frac{2\nu}{H_2^2} + \frac{2\beta x_2 H_2^2}{\nu L^2} + \frac{2\gamma y_2 H_2^2}{\nu \ell^2} \right)^2 H_2^2 \delta^2. \quad (\text{A } 3)$$

This means nothing else than $U_{3D}^2 \propto \delta^2$, which is precisely the scaling observed in figure 8b. It is important to note however that the asymptotic result (A 3) is only valid for very small δ and cannot be extended to $\delta \sim O(1)$ where the quadratic terms are dominant.

REFERENCES

- ALEXAKIS, ALEXANDROS 2011 Two-dimensional behavior of three-dimensional magnetohydrodynamic flow with a strong guiding field. *Physical Review E* **84** (5), 056330.
- ALEXAKIS, ALEXANDROS 2015 Rotating Taylor–Green flow. *Journal of Fluid Mechanics* **769**, 46–78.
- ALEXAKIS, ALEXANDROS 2018 3d instabilities and negative eddy viscosity in thin-layer flows. *arXiv preprint arXiv:1806.00409*.
- BARTELLO, PETER, MÉTAIS, OLIVIER & LESIEUR, MARCEL 1994 Coherent structures in rotating three-dimensional turbulence. *Journal of Fluid Mechanics* **273**, 1–29.
- BENAVIDES, SANTIAGO JOSE & ALEXAKIS, ALEXANDROS 2017 Critical transitions in thin layer turbulence. *Journal of Fluid Mechanics* **822**, 364385.
- BOFFETTA, GUIDO & ECKE, ROBERT E. 2012 Two-dimensional turbulence. *Annual Review of Fluid Mechanics* **44** (1), 427–451, arXiv: <https://doi.org/10.1146/annurev-fluid-120710-10124>.
- BOUCHET, FREDDY & SIMONNET, ERIC 2009 Random changes of flow topology in two-dimensional and geophysical turbulence. *Physical review letters* **102** (9), 094504.
- CAMERON, ALEXANDRE, ALEXAKIS, ALEXANDROS & BRACHET, MARC-ÉTIENNE 2016 Large-scale instabilities of helical flows. *Physical Review Fluids* **1** (6), 063601.
- CAMERON, ALEXANDRE, ALEXAKIS, ALEXANDROS & BRACHET, MARC-ÉTIENNE 2017 Effect of helicity on the correlation time of large scales in turbulent flows. *Physical Review Fluids* **2** (11), 114602.
- CELANI, ANTONIO, MUSACCHIO, STEFANO & VINCENZI, DARIO 2010 Turbulence in more than two and less than three dimensions. *Phys. Rev. Lett.* **104**, 184506.
- DALLAS, VASSILIOS, FAUVE, STEPHAN & ALEXAKIS, ALEXANDROS 2015 Statistical equilibria of large scales in dissipative hydrodynamic turbulence. *Physical review letters* **115** (20), 204501.
- DEUSEBIO, ENRICO, BOFFETTA, GUIDO, LINDBORG, ERIK & MUSACCHIO, STEFANO 2014 Dimensional transition in rotating turbulence. *Physical Review E* **90** (2), 023005.
- DUBRULLE, BÉRENGÈRE & FRISCH, URIEL 1991 Eddy viscosity of parity-invariant flow. *Phys. Rev. A* **43**, 5355–5364.
- FRISCH, URIEL 1995 *Turbulence: the legacy of AN Kolmogorov*. Cambridge university press.

- FRISHMAN, ANNA & HERBERT, CORENTIN 2017 Turbulence statistics in a 2d vortex condensate. *arXiv preprint arXiv:1711.05536* .
- FRISHMAN, ANNA, LAURIE, JASON & FALKOVICH, GREGORY 2017 Jets or vortices what flows are generated by an inverse turbulent cascade? *Physical Review Fluids* **2** (3), 032602.
- FUJISAKA, HIROKAZU & YAMADA, TOMOJI 1985 A new intermittency in coupled dynamical systems. *Progress of theoretical physics* **74** (4), 918–921.
- GALLET, BASILE & DOERING, CHARLES R. 2015 Exact two-dimensionalization of low-magnetic-reynolds-number flows subject to a strong magnetic field. *Journal of Fluid Mechanics* **773**, 154177.
- GAMA, S, VERGASSOLA, M & FRISCH, U 1994 Negative eddy viscosity in isotropically forced two-dimensional flow: linear and nonlinear dynamics. *Journal of fluid mechanics* **260**, 95–126.
- KRAICHNAN, ROBERT H 1973 Helical turbulence and absolute equilibrium. *Journal of Fluid Mechanics* **59** (4), 745–752.
- KRAICHNAN, ROBERT H 1976 Eddy viscosity in two and three dimensions. *Journal of the atmospheric sciences* **33** (8), 1521–1536.
- MARINO, R, POUQUET, A & ROSENBERG, D 2015 Resolving the paradox of oceanic large-scale balance and small-scale mixing. *Physical review letters* **114** (11), 114504.
- MESHALKIN, LD 1962 Investigation of the stability of a stationary solution of a system of equations for the plane movement of an incompressible viscous liquid. *J. Appl. Math. Mech.* **25**, 1700–1705.
- MININNI, PABLO D, ROSENBERG, DUANE, REDDY, RAGHU & POUQUET, ANNICK 2011 A hybrid mpi–openmp scheme for scalable parallel pseudospectral computations for fluid turbulence. *Parallel Computing* **37** (6-7), 316–326.
- MUSACCHIO, STEFANO & BOFFETTA, GUIDO 2017 Split energy cascade in turbulent thin fluid layers. *Physics of Fluids* **29** (11), 111106.
- PEDLOSKY, JOSEPH 2013 *Geophysical fluid dynamics*. Springer Science & Business Media.
- PLATT, N., SPIEGEL, E. A. & TRESSER, C. 1993 On-off intermittency: A mechanism for bursting. *Phys. Rev. Lett.* **70**, 279–282.
- RAVELET, FLORENT, MARIÉ, LOUIS, CHIFFAUDEL, ARNAUD & DAVIAUD, FRANÇOIS 2004 Multistability and memory effect in a highly turbulent flow: Experimental evidence for a global bifurcation. *Phys. Rev. Lett.* **93**, 164501.
- SAHOO, GANAPATI, ALEXAKIS, ALEXANDROS & BIFERALE, LUCA 2017 Discontinuous transition from direct to inverse cascade in three-dimensional turbulence. *Physical review letters* **118** (16), 164501.
- SAHOO, GANAPATI & BIFERALE, LUCA 2015 Disentangling the triadic interactions in navier-stokes equations. *The European Physical Journal E* **38** (10), 114.
- SESHASAYANAN, KANNABIRAN & ALEXAKIS, ALEXANDROS 2016 Critical behavior in the inverse to forward energy transition in two-dimensional magnetohydrodynamic flow. *Physical Review E* **93** (1), 013104.
- SESHASAYANAN, KANNABIRAN & ALEXAKIS, ALEXANDROS 2018 Condensates in rotating turbulent flows. *Journal of Fluid Mechanics* **841**, 434–462.
- SESHASAYANAN, KANNABIRAN, BENAVIDES, SANTIAGO JOSE & ALEXAKIS, ALEXANDROS 2014 On the edge of an inverse cascade. *Physical Review E* **90** (5), 051003.
- SIVASHINSKY, G & YAKHOT, V 1985 Negative viscosity effect in large-scale flows. *The Physics of fluids* **28** (4), 1040–1042.
- SMITH, LESLIE M, CHASNOV, JEFFREY R & WALEFFE, FABIAN 1996 Crossover from two-to three-dimensional turbulence. *Physical review letters* **77** (12), 2467.
- SOZZA, ALESSANDRO, BOFFETTA, GUIDO, MURATORE-GINANNESCHI, P & MUSACCHIO, STEFANO 2015 Dimensional transition of energy cascades in stably stratified forced thin fluid layers. *Physics of Fluids* **27** (3), 035112.
- WEEKS, ERIC R, TIAN, YUDONG, URBACH, JS, IDE, KAYO, SWINNEY, HARRY L & GHIL, MICHAEL 1997 Transitions between blocked and zonal flows in a rotating annulus with topography. *Science* **278** (5343), 1598–1601.
- YAKHOT, V. & SIVASHINSKY, G. 1987 Negative-viscosity phenomena in three-dimensional flows. *Phys. Rev. A* **35**, 815–820.
- YOKOYAMA, NAOTO & TAKAOKA, MASANORI 2017 Hysteretic transitions between quasi-two-

dimensional flow and three-dimensional flow in forced rotating turbulence. *Physical Review Fluids* **2** (9), 092602.